Electrical manipulation of ferromagnetic NiFe by antiferromagnetic IrMn

V. Tshitoyan,[1] C. Ciccarelli,[1] A. P. Mihai,[2,*] M. Ali,[2] A. C. Irvine,[1] T. A. Moore,[2] T. Jungwirth,[3,4] and A. J. Ferguson[1,†]

[1]*Microelectronics Group, Cavendish Laboratory, University of Cambridge, CB3 0HE, United Kingdom*

[2]*School of Physics and Astronomy, University of Leeds, Leeds LS2 9JT, United Kingdom*

[3]*Institute of Physics ASCR, v.v.i., Cukrovarnická 10, 162 53 Praha 6, Czech Republic*

[4]*School of Physics and Astronomy, University of Nottingham, Nottingham NG7 2RD, United Kingdom*

(Received 22 September 2015; revised manuscript received 9 November 2015; published 3 December 2015)

We demonstrate that an antiferromagnet can be employed for a highly efficient electrical manipulation of a ferromagnet. In our study, we use an electrical detection technique of the ferromagnetic resonance driven by an in-plane ac current in a NiFe/IrMn bilayer. At room temperature, we observe antidampinglike spin torque acting on the NiFe ferromagnet, generated by an in-plane current driven through the IrMn antiferromagnet. A large enhancement of the torque, characterized by an effective spin-Hall angle exceeding most heavy transition metals, correlates with the presence of the exchange-bias field at the NiFe/IrMn interface. It highlights that, in addition to the strong spin-orbit coupling, the antiferromagnetic order in IrMn governs the observed phenomenon.

DOI: 10.1103/PhysRevB.92.214406 PACS number(s): 85.75.−d, 72.25.−b, 76.50.+g, 75.76.+j

I. INTRODUCTION

Recently, a new direction in spintronics has been proposed based on nonrelativistic [1–5] and relativistic [6,7] spin-transport phenomena in which antiferromagnets (AFMs) complement or replace ferromagnets (FMs) in active parts of the device. AFMs have for decades played a passive role in conventional spin-valve structures where they provide pinning of the reference FM layer [8]. This implies that the incorporation of some AFM materials, including IrMn, in common spintronic structures is well established. On the other hand, limiting their utility to a passive pinning role, leaves a broad range of spintronic phenomena and functionalities based on AFMs virtually unexplored. In addition to the insensitivity to magnetic fields and the lack of stray fields, AFMs are common among metals, semiconductors, and insulators and can have orders of magnitude shorter spin-dynamics time scales, to name a few immediate merits of the foreseen concept of AFM spintronics.

Antiferromagnetic magnetoresistor and memory functionalities have been demonstrated by manipulation of the AFM moments via a FM sensitive to external magnetic fields [9–12]. Wadley *et al.* [13] showed that in AFMs with a specific crystal and magnetic structures, AFM moments can be manipulated electrically. Several studies have also focused on transmission and detection of spin-currents in AFMs. In FM/AFM/normal-metal (NM) trilayers, a spin current was pumped from the FM, detected by the inverse spin-Hall effect (ISHE) in the NM, and the observed robust spin transport through the interfacial AFM (insulating NiO) was ascribed to AFM moment fluctuations [14,15]. Efficient spin transmission through an AFM (IrMn) was also inferred from an inverse experiment in the FM/AFM/NM structure [16] in which a spin current was generated by the spin-Hall effect (SHE) in the NM and absorbed via the spin transfer torque (STT) [17] in the FM. Measurements in FM/AFM bilayers have demonstrated that a metallic AFM itself (e.g., IrMn) can act as an efficient ISHE detector of the spin current injected from the FM, with comparable spin-Hall angles to heavy NMs [18,19].

Our work makes the next step beyond previous studies of transmission and detection of spin currents in AFMs by focusing on spin manipulation by AFMs. In a NiFe/Cu/IrMn structure, we demonstrate that the IrMn AFM produces a large SHE spin current, which is transmitted through Cu and exerts an antidampinglike STT on the NiFe FM comparable in strength to the SHE-STT generated by Pt. Upon removing the interfacial Cu layer, we observe that the size of the antidampinglike torque is strongly enhanced and that it correlates with the exchange-bias field associated with the fixed AFM moments at the coupled NiFe/IrMn interface. Our observations point to new physics and functionalities that AFMs can bring to the currently highly active research area of relativistic spin-orbit torques induced by in-plane currents in inversion asymmetric magnetic structures [20–28].

In the next section, we describe the experimental technique and present the measurements of the current-induced torques in a sample with 2-nm IrMn with no Cu spacer, compared to a sample without IrMn. In Sec. III, we present measurements in structures with different IrMn thicknesses, Cu spacers, as well as different temperatures, demonstrating the enhancement of the torque in the presence of the exchange bias. In Sec. IV, we discuss the possible microscopic origins of the observed enhancement, followed by a conclusion in Sec. V.

II. OBSERVATION OF THE ANTIDAMPING TORQUE

Multilayers SiO_x/Ru(3)/IrMn(d_A)/NiFe(4)/Al(2) and SiO_x/Ru(3)/IrMn(4)/Cu(d_N)/NiFe(4)/Al(2) used in our measurements were grown using dc magnetron sputtering. The numbers represent layer thicknesses in nanometers. The IrMn thickness d_A in the first type of multilayers varies from 0–12 nm, and Cu thickness d_N in the second type of multilayers is 1 or 2 nm. We apply microwave (MW) frequency electrical current to a bar patterned from the magnetic multilayer. Bars used in our measurements vary from 500 nm to 4 μm in width and 5 to 240 μm in length. The torques induced by the oscillating current in the bar drive the magnetization

*Currently at London Centre for Nanotechnology, Department of Materials, Imperial College London, SW7 2BP, United Kingdom.

†ajf1006@cam.ac.uk

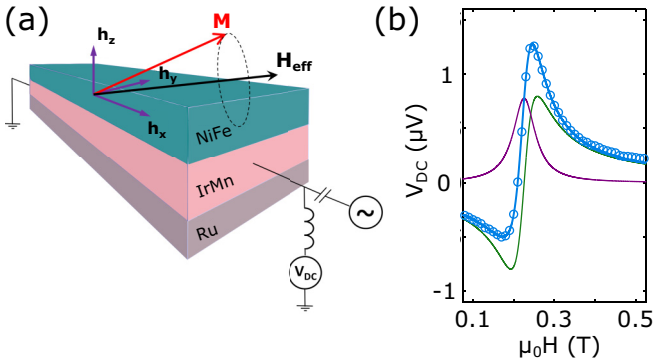

FIG. 1. (Color online) Spin-orbit FMR experiment. (a) Schematic representation of the measurement technique. MW current-induced effective field $\mathbf{h}(h_x,h_y,h_z)$ drives magnetization precession around the total field $\mathbf{H}_{\text{eff}}$. Precessing magnetization results in oscillating resistance due to AMR. This mixes with the oscillating current of the same frequency resulting in a measurable dc voltage. (b) Resonance curve decomposed into symmetric and antisymmetric components measured in a bar with 2-nm IrMn at frequency of 17.9 GHz.

precession of the NiFe around the equilibrium axis defined by an applied saturating magnetic field. A diagram of the measurement setup and the device is shown in Fig. 1(a). The bar is aligned along the x axis, while the z axis represents the out-of-plane direction. The resonant precession is detected as a rectified dc voltage due to the anisotropic magnetoresistance (AMR) [29]. In our studies, we keep the frequency of the current constant and sweep the in-plane magnetic field [Fig. 1(b)]. From the decomposition of the resonance into symmetric and antisymmetric Lorentzians [23], we deduce the out-of-plane and in-plane components of the driving field as

$$V_{\text{sym}} = \frac{I\Delta R}{2} A_{\text{sym}} h_z \sin 2\theta, \tag{1}$$

$$V_{\text{asy}} = \frac{I\Delta R}{2} A_{\text{asy}} (h_y \cos\theta - h_x \sin\theta) \sin 2\theta. \tag{2}$$

Here, I is the current in the bar, ΔR is the AMR amplitude, A_{sym} and A_{asy} are coefficients determined by the magnetic anisotropies, and θ is the angle between the magnetization and current directions. Current-induced fields h_x, h_y, and h_z can be obtained from the measured angle dependencies of V_{sym} and V_{asy}. We calibrate the microwave current I in the bar from the resistance change induced by microwave heating (Appendix A). ΔR is obtained from the in-plane AMR measurement using a 1-T magnetic field, while the anisotropy coefficients A_{sym} and A_{asy} are extracted from the angle dependence of the resonance field (Appendix E).

In Fig. 2(a), we compare the resonance curves for samples without the Cu layer and with 0 and 2 nm thick IrMn. The resonance is predominantly antisymmetric without IrMn, indicating a driving field in the in-plane direction. The resonance then acquires a substantial symmetric component in the presence of the AFM, indicating an additional driving field in the out-of-plane direction. Both symmetric and antisymmetric components follow a $\sin 2\theta \cos\theta$ angle dependence [Fig. 2(b)].

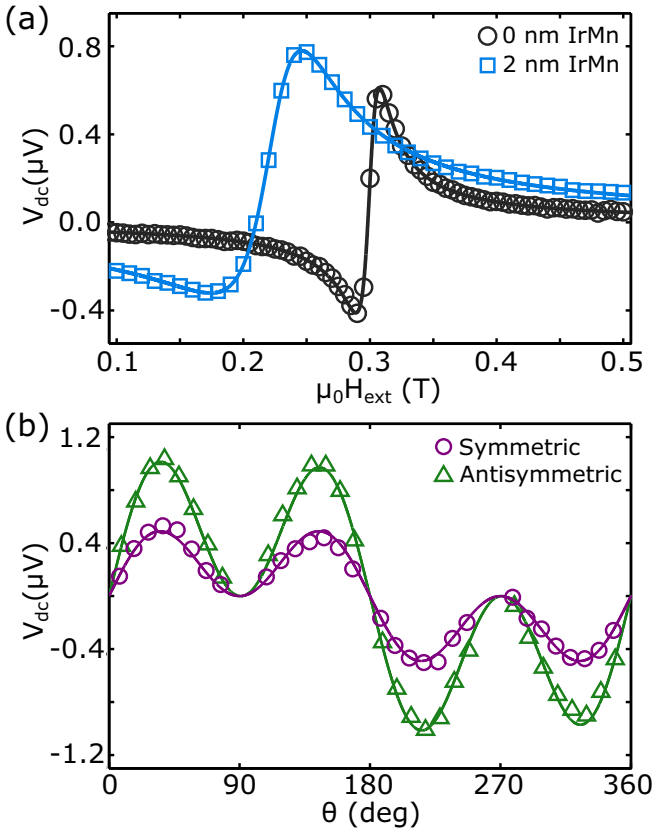

FIG. 2. (Color online) AFM-induced torque and its symmetries. (a) Comparison of resonance curves measured in samples with and without the IrMn layer. Both measurements are performed at 17.9 GHz, $\theta = 45°$. Antisymmetric components are normalized to 1 μV. (b) Symmetries of V_{sym} and V_{asy} for the sample with 2-nm IrMn. Solid lines are fits to Eqs. (1) and (2).

This means that the in-plane effective field is along the y direction and is independent on the magnetization direction, resulting in an out-of-plane field-like torque, $\tau_{\mathbf{z}} \propto \mathbf{m} \times \hat{\mathbf{y}}$. In contrast, h_z depends on the magnetization direction as $\cos\theta \propto [\mathbf{j} \times \hat{\mathbf{z}}] \times \mathbf{m}$, thus resulting in an antidampinglike in-plane torque $\tau_{\mathbf{ad}} \propto \mathbf{m} \times ([\mathbf{j} \times \hat{\mathbf{z}}] \times \mathbf{m})$. It is important to note here that the observed ratios of symmetric and antisymmetric Lorentzians, and subsequently of h_z and h_y are independent on microwave power, frequency, and sample dimensions (Appendix D).

We find that for all our samples the magnitude of h_y is compatible with the magnitude of the Oersted field induced by the current in IrMn, Cu, and Ru layers. The Oersted field is calculated using the individual layer resistivities extracted from resistance measurements of bars with different layer thicknesses (Appendix B). From the fits of the symmetric and antisymmetric components to Eqs. (1) and (2) shown in Fig. 2(b), we deduce $\mu_0 h_z = 1.13 \pm 0.05$ mT and $\mu_0 h_y = 1.04 \pm 0.03$ mT, while for the Oersted field, we find $\mu_0 h_{\text{Oe}} = 1.09 \pm 0.07$ mT. All values reported for the current-induced fields are normalized to a current density of 10^7 A/cm^2 in IrMn. The symmetry of h_z is compatible both with the antidampinglike term of the interface-induced Rashba spin-orbit torque [24,25], as well as with the SHE-STT [26]. In the

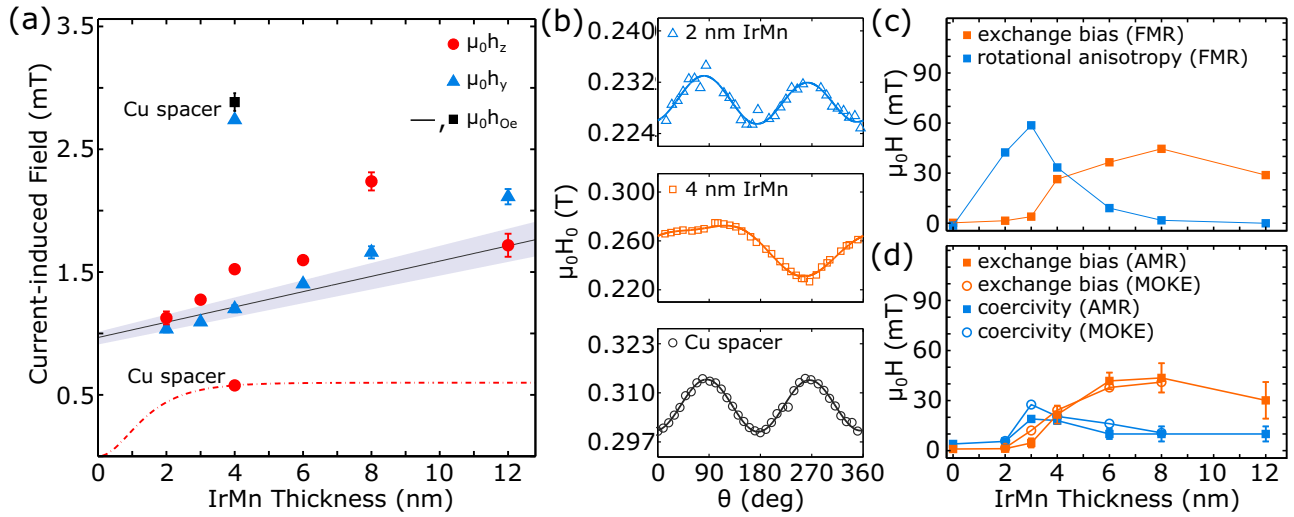

FIG. 3. (Color online) AFM thickness dependence of current-induced fields and anisotropies. (a) h_z, h_y, and calculated Oersted field h_{Oe} for 1.8-μm wide bars with different IrMn thicknesses, as well as the sample with the 2-nm Cu spacer layer. The results are normalized to a current density of 10^7 A/cm^2 in IrMn. The shaded area around h_{Oe} is the error due to uncertainties in layer resistivities, whereas the error bars of h_z and h_y are due to the standard errors from the fitting of the symmetries, AMR and MW current. The systematic uncertainties in layer resistivities have not been included in the error bars of h_z and h_y, however, this uncertainty, which is approximately 20%, is included in the values of effective spin-Hall angles in the main text. The dotted line is the estimated spin-Hall effect contribution to h_z for $\lambda_{sd} = 1$ nm. (b) Angle dependencies of resonance field for the samples with 2- and 4-nm IrMn thicknesses, as well as the sample with the 2-nm Cu spacer layer. Solid lines are fits taking into account unidirectional, uniaxial and rotational anisotropies. (c) IrMn thickness dependence of the exchange bias and the rotational anisotropy extracted from the fits in (a). (d) IrMn thickness dependence of exchange bias and coercivity extracted from hysteresis loops measured using MOKE and AMR switching.

latter case the spin-current generated in the IrMn by the SHE drives magnetization precession in the NiFe layer by STT. Both of these effects occur in FM/NM structures, however, we show that additional effects arise due to the AFM nature of IrMn and the exchange coupling at the FM/AFM interface.

III. ORIGINS OF THE EFFECT

To separate the contribution of the exchange-coupled NiFe/IrMn from the SHE-STT, we perform measurements in samples with 4-nm-thick IrMn, and 1- and 2-nm-thick Cu spacers between IrMn and NiFe. Cu has a spin-diffusion length of 350 nm [30] and thus 2 nm of Cu would transfer >99% of the spin-Hall current from IrMn, but eliminate the FM/AFM coupling [31] and the FM/AFM interface-induced effects.

Results obtained in samples with the Cu spacer and without Cu and different IrMn thicknesses are summarized in Fig. 3(a). Firstly, one can see that the h_z field does not vanish with the introduction of Cu, indicating the SHE in IrMn. From the value of h_z, we can obtain the spin-Hall angle θ_{SH} of IrMn from the expression

$$\theta_{\mathrm{SH}} = \frac{2e\mu_0 M_s d_F}{\hbar J_{\mathrm{IrMn}}} h_z. \tag{3}$$

Here, $d_F = 4$ nm is the thickness of the NiFe layer, $\mu_0 M_s = 1$ T is the saturation magnetization of NiFe, $J_{\mathrm{IrMn}} = 10^7$ A/cm^2 is the charge current density in IrMn and $\mu_0 h_z = 0.58 \pm 0.02$ mT is obtained from the measurement. We get $\theta_{\mathrm{IrMn}} = 0.056 \pm 0.009$, in good agreement with the expected value for $Ir_{25}Mn_{75}$ [18]. Here the uncertainty also includes the uncertainty of the current density in IrMn from the layer resistivity calibration. It is important to mention that the same value of θ_{IrMn} was obtained for both 1-nm and 2-nm Cu spacers, as well as bars with 1.8-μm and 500-nm widths. Remarkably, in addition to the SHE, we see a large contribution from the FM/AFM interface in samples without Cu, initially increasing with the IrMn thickness and with a peak at 8 nm of IrMn, with a magnitude corresponding to an effective spin-Hall angle of 0.22 ± 0.04. The values of effective spin-Hall angles for two samples, as well as the dampinglike nature of h_z were confirmed by measuring the dc bias dependence of the FMR linewidth [32]. Depending on the direction of dc current with respect to FM magnetizaion, an additional damping or antidamping is induced, thereby increasing or decreasing the FMR linewidth. For the sample with the Cu spacer, we obtain $\theta_{\mathrm{SH}} = 0.043 \pm 0.001$ [Fig. 4(a)] and for the sample with 2-nm IrMn, we get $\theta_{\mathrm{SH}} = 0.135 \pm 0.022$ [Fig. 4(b)]. We use

$$\theta_{\mathrm{SH}} = \frac{\partial(\mu_0 \Delta H)}{\partial(j_{\mathrm{IrMn}})} \frac{\gamma}{\omega} \frac{2e}{\hbar} \frac{(H_{\mathrm{res}} + M_{\mathrm{eff}}/2)\mu_0 M_s t_{\mathrm{NiFe}}}{\sin\theta}, \tag{4}$$

where the first term is the slope of the linear fit with respect to the current density in IrMn. For comparison, the values obtained using the magnitude of h_z extracted from our FMR measurements [Fig. 3(a)] are 0.056 ± 0.001 for the sample with the Cu spacer and 0.109 ± 0.005 for the 2-nm IrMn sample. The values are in a good agreement if we also include the resistivity calibration error of approximately 20% in addition to the uncertainties from the fitting.

We note here that in a recent study, Moriyama *et al.* [16] used similar FM/AFM/NM structures but instead of Ru they had Pt NM. Unlike our results, the introduction of the interfacial IrMn AFM in Moriyama *et al.* structures always

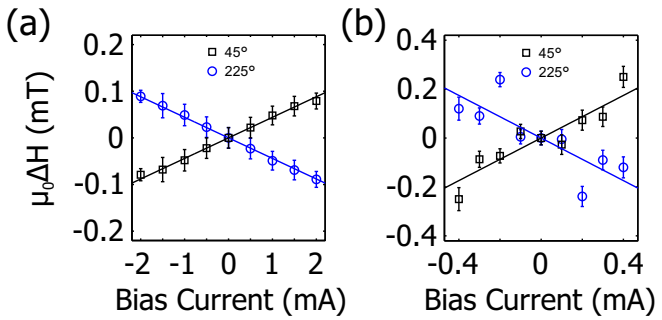

FIG. 4. (Color online) DC bias dependence of the FMR linewidth. (a) Change of FMR linewidth with dc current for the IrMn(4)/Cu(2)/NiFe(4) structure measured at $\omega/2\pi = 8$ GHz and (b) IrMn(2)/NiFe(4) structure measured at $\omega/2\pi = 14.1$ GHz, for two different directions of magnetization with respect to the current. The data points are extracted using the linewidth difference between positive and negative bias currents.

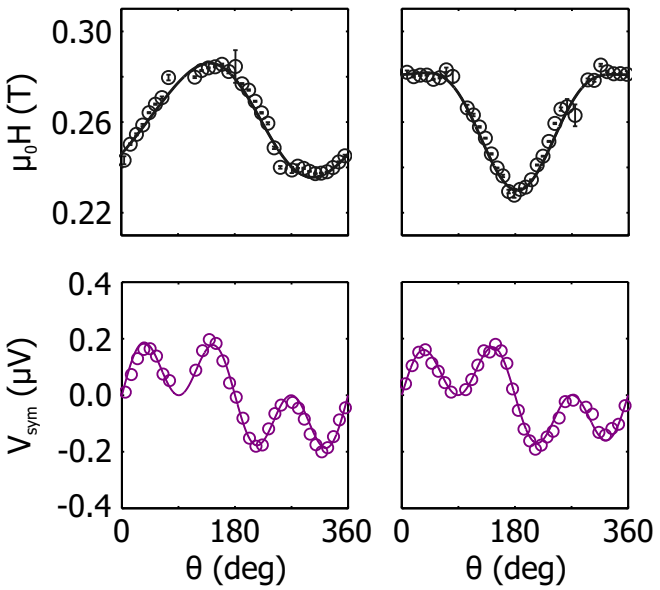

FIG. 5. (Color online) Independence on the exchange bias direction. Angle dependence of the resonance field for two different 4-nm IrMn bars (top) and corresponding symmetric components of the measured dc voltage (bottom). Although the exchange bias is substantial and has different directions for the two bars, the angle dependence of the symmetric component of the Lorentzian, corresponding to h_z, is not affected.

reduced the spin torque, compared to the reference FM/NM sample without the AFM. The authors concluded that in their case, the SHE in the AFM did not play a significant role and that the observed torque was due to the spin-Hall current from Pt transferred to the FM via spin-waves in the AFM. In our case, Ru has a small spin-Hall angle [33], which we find from the control sample without IrMn to be ≈0.009 (Appendix E). This, given the current distribution in the multilayer, would have a contribution of $h_z \approx 0.48$ mT in all the samples. Even if we assumed that the spin-angular momentum carried by the spin-Hall current from the Ru layer is fully transferred through IrMn, it would still be too small to explain the effect in samples with IrMn thicknesses larger than 3 nm, as seen in Fig. 3(a). Additionally, we performed measurements in samples with Ta seed layers instead of Ru, and found a large positive h_z similar to the Ru samples ($h_z/h_y \approx 0.9$). Ta has a large negative spin-Hall angle and one would expect a negative or a largely suppressed h_z if the seed layer had a significant contribution (Appendix E).

The increase of the antidampinglike torque in our NiFe/IrMn samples with increasing IrMn thickness cannot be explained by the increase in the spin-Hall current, as shown by the dotted line in Fig. 3(a), because IrMn has a spin diffusion length smaller than 1 nm [19,34]. It is clearly associated with the exchange-coupled NiFe/IrMn interface. The two leading anisotropies commonly used to characterize FM/AFM interfaces are the exchange bias field and the rotational anisotropy, the latter being the origin of the increased coercivity [35,36]. Rotational anisotropy can be modelled as an additional effective field along the magnetization direction, and thus results in an overall decrease of the resonance field in FMR measurements. This decrease is seen in Fig. 2(a). The anisotropies are quantified from the angle dependence of the resonance field, plotted in Fig. 3(b) for the 2- and 4-nm IrMn samples and the sample with 2-nm Cu spacer, all measured at 17.9 GHz. Comparing the top graph (2-nm IrMn with no spacer) and the bottom graph (2 nm Cu spacer), we see a smaller resonance field in the sample with 2-nm IrMn due to the rotational anisotropy induced at the FM/AFM interface, as discussed earlier. For the thicker IrMn sample (middle graph), a unidirectional contribution due to the exchange bias has developed.

Thickness dependencies of the exchange bias field H_{ex} and the rotational anisotropy field H_{rot} extracted from the fits are plotted in Fig. 3(c) and compared to H_{ex} and H_c extracted from MOKE and AMR switching measurements plotted in Fig. 3(d), showing a good agreement. One can see the onset of exchange bias at 3 nm and a peak at 8 nm of IrMn. The rotational anisotropy and coercivity are the largest for the sample with 3-nm IrMn. Similar thickness dependence has been observed experimentally using different techniques [37,38]. One can see a correlation between the size of the exchange bias and h_z by comparing Figs. 3(a), 3(c), and 3(d). It is worth mentioning here that although the exchange bias has different directions for 4–12-nm IrMn samples the symmetry of h_z is not affected by it (Fig. 5).

To confirm the correlation between the antidampinglike torque and exchange bias in one sample, we perform temperature dependence measurements of the h_z/h_y ratio for the sample with 2-nm IrMn. Although this ratio is not a direct measure of the effective spin-Hall angle due to the possible current redistribution with temperature, it can help with the qualitative understanding. The results are shown in Fig. 6(a).

The monotonous decrease in the h_z/h_y ratio down to 50 K can be explained with the current redistribution in the bar. IrMn is an alloy, and thus its resistivity decreases less with temperature compared to Ru, resulting in a smaller proportion of current flowing through IrMn, and thus smaller h_z at lower temperatures. The ratio can also change monotonously with temperature if there are additional temperature dependent

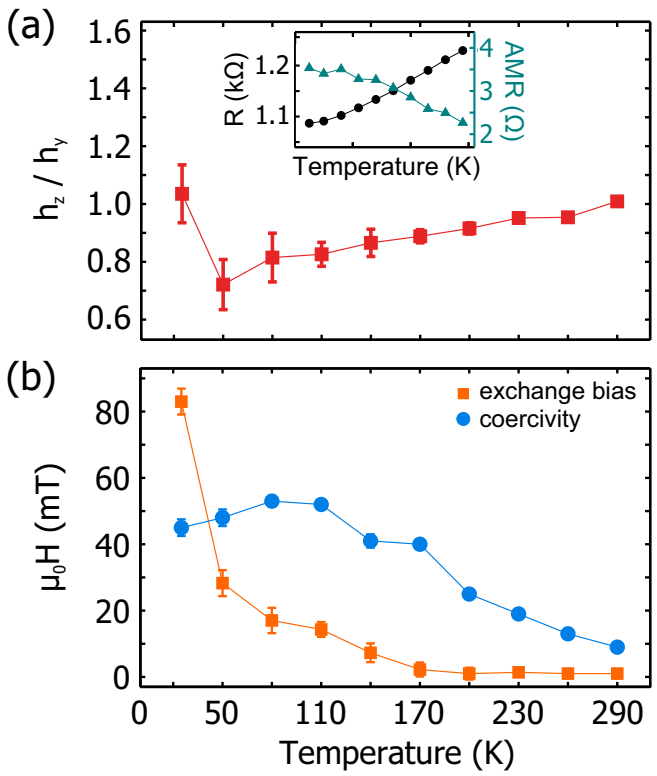

FIG. 6. (Color online) Temperature dependence of current-induced fields and anisotropies. (a) Temperature dependence of the h_z/h_y ratio for the sample with 2-nm IrMn. The inset shows the temperature dependence of the AMR and total resistance of the bar. (b) Temperature dependence of the exchange bias and the coercivity for the same sample extracted from AMR switching measurements.

contributions to h_y [39]. Nevertheless, as one can see the monotonic trend is broken below 50 K, coinciding with the abrupt increase in the exchange bias and decrease in the coercivity [Fig. 6(b)]. In the inset of Fig. 6(a), we plot the change of resistance and AMR with temperature, showing their monotonous behavior for the whole temperature range. This result is significant because it shows dependence of current-induced torques on AFM-induced anisotropies in a single device. We also found that cooling down the sample from room temperature to 25 K with applied 1-T magnetic field along different directions changes the direction of the exchange bias, however, this does not significantly change magnitudes and symmetries of the current-induced fields.

IV. DISCUSSION

The origin of relativistic spin torques induced by an in-plane current at FM/NM interfaces is a subject of current intense theory discussions. Our results clearly indicate that replacing the NM with an AFM adds to the richness of these phenomena which inevitably brings more complexity to their theoretical description. To stimulate future detailed microscopic analyses, we outline here possible mechanisms that might be considered as the origin of the enhancement of the antidampinglike torque and its correlation with the exchange bias. Firstly, the exchange coupling could increase the transparency at the FM/AFM interface resulting in a more efficient spin transfer. One can estimate the efficiency of spin-transfer through FM/NM interface from the frequency dependence of the FMR linewidth [40]. This is characterized by the effective Gilbert damping α, extracted from the slope in Fig. 7(a). In Fig. 7(b), we plot h_z as a function of α for the samples with different IrMn thicknesses. One can see a clear linear trend, suggesting that h_z is correlated with the spin-angular momentum transfer properties through the interface. Additionally, in Fig. 7(c), we show that the enhancement of the spin-angular momentum transfer through the interface is indeed due to the interfacial exchange coupling, as α is proportional to the square of the exchange bias. This dependence also suggest that one of the main damping mechanisms in our samples is the two-magnon scattering at the FM/AFM interface, in agreement with the previous studies [19,41,42]. The exact mechanism of the enhancement of h_z is of complex origin due to the strong spin-orbit coupling in the system and the interface magnetic coupling. If we assume that the damping enhancement is merely due to more efficient spin-pumping and try to estimate the value of the transparency at the interface in the weak

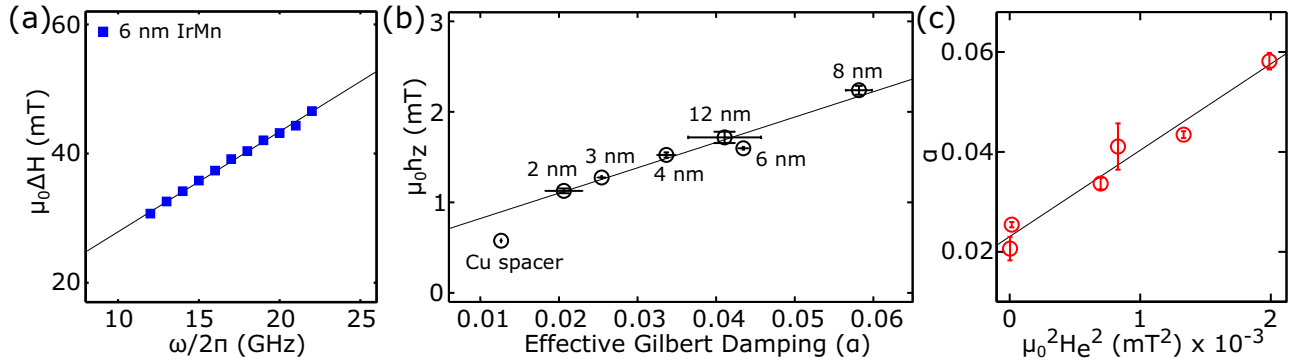

FIG. 7. (Color online) AFM-induced torque and Gilbert damping. (a) Frequency dependence of the FMR linewidth for the sample with 6-nm IrMn. The slope of the linear fit allows us to extract the effective Gilbert damping $\alpha = \gamma\mu_0(\partial\Delta H/\partial\omega)$, where $\gamma/2\pi = 28$ GHz/T. (b) Current-induced out-of-plane field h_z plotted against the effective Gilbert damping for samples with different IrMn thicknesses. (c) Gilbert damping is proportional to the square of the exchange bias, suggesting that one of the main damping mechanisms in our samples is the two-magnon scattering due to the inhomogeneity of the field at the FM/AFM interface induced by the exchange anisotropy.

spin-orbit coupling picture of spin-mixing conductance using [40]

$$G_{\mathrm{mix}} = \frac{G_{\mathrm{eff}}}{1 - 2G_{\mathrm{eff}}\lambda_{SD}/\sigma_{\mathrm{IrMn}}}, \tag{5}$$

where

$$G_{\mathrm{eff}} = \frac{e^2}{h}\frac{4\pi M_s d_F}{g\mu_B}(\alpha - \alpha_0), \tag{6}$$

using values $\lambda_{SD} = 0.7$ nm [19] and conductivity $\sigma_{\mathrm{IrMn}} = 1/\rho_{\mathrm{IrMn}}$, we obtain negative values for G_{mix}, which is nonphysical. Here, $\alpha_0 = 0.006$ is the Gilbert damping of bulk NiFe. One would have to assume $\lambda_{SD} < 0.1$ nm to obtain positive G_{mix}. This additionally suggests that the mechanism of the damping enhancement, and subsequently the torque enhancement is more complex than just an increase of spin-current transparency at the interface combined with the spin-Hall effect.

Another possibility is that additional torques are induced directly at the FM/AFM interface, or induced in the AFM and coupled to the FM via the exchange interaction. In this case, the level of the magnetic order in the AFM layer, as well as the interface roughness could be important for the size of the torque. Wei *et al.* [43] and Urazhdin *et al.* [44] observed changes in exchange bias in current perpendicular-to-plane geometries, attributed to torques changing the AFM magnetic structure at the FM/AFM interface. We note that our measurement is not sensitive to the bulk AFM magnetic order, except through its correlation with the exchange bias at the interface. We also point out that we use 2–3 orders of magnitude lower in-plane currents compared to Refs. [43,44], avoiding heating effects and employing a different current path geometry which excludes the possibility of a direct comparison between the experiments. A more detailed theoretical investigation is needed to determine the exact microscopic mechanism of the enhanced antidamping torques, given the complex nature of the system.

V. CONCLUSIONS

In conclusion, we have shown that electrical current in the IrMn AFM induces a large torque acting on the adjacent NiFe FM. The torque is in-plane and has an antidampinglike symmetry. We have also shown that there are at least two distinct contributions, one coming from the SHE in IrMn, and the other due to the AFM order of IrMn. The spin-Hall angle of IrMn measured in the sample with the Cu spacer between NiFe and IrMn is found to be 0.056 ± 0.009, comparable to that of Pt. An effective spin-Hall angle of 0.22 ± 0.04, almost three times larger than that of Pt, is measured for the sample with 8-nm IrMn in direct contact with NiFe, exhibiting the largest exchange bias. Our results suggest that electrical current in AFMs can induce torques more efficiently than in most of the heavy NMs. The AFM-induced torques and their correlation with the exchange coupling at the FM/AFM interface could lead to novel designs of spintronic devices. After completing our work we learned about a related study on electrical manipulation of magnetization dynamics in a ferromagnet by antiferromagnets [45].

VI. METHODS AND MATERIALS

Materials. The structures were grown using dc magnetron sputtering on a thermally oxidized Si (100) substrate. In-plane magnetic field of 200 Oe was applied during growth. The polycrystalline IrMn is believed to be 111 textured for the structures to exhibit such large exchange bias at room temperature [37].

Devices. The microbars are patterned using electron-beam lithography. In Figs. 2, 5, and 6 we show measurements done in bars with 500-nm width and 5-μm length, whereas the measurements shown in Fig. 3 are done in bars with 1.8×38 μm dimensions. Measurements in Figs. 2 and 3 are repeated in at least two bars with different dimensions. The results are consistent across different bars and all the bar dimensions. The resistivity calibration measurements are done in 4-μm wide bars with 40, 80, 120, and 240 μm lengths. Typical resistances are on the order of 1 kΩ for bars with length to width ratios of 10.

Experimental procedure. For more details on the methods related to our SO-FMR experiments see Refs. [23,28].

VII. ADDITIONAL INFORMATION

Correspondence and requests for materials should be addressed to AJF (ajf1006@cam.ac.uk).

ACKNOWLEDGMENTS

Authors would like to acknowledge Hidekazu Kurebayashi and Tim Skinner for useful discussions. We acknowledge support from the EU European Research Council (ERC) Advanced Grant No. 268066, the Ministry of Education of the Czech Republic Grant No.LM2011026, and the Grant Agency of the Czech Republic Grant No. 14-37427G. VT would like to acknowledge Alexander Baker for useful discussions on Gilbert damping, as well as Winton Programme for the Physics of Sustainability and Cambridge Overseas Trusts for financial support.

APPENDIX A: MICROWAVE CURRENT CALIBRATION

Resistances of measured bars vary between a few 100 Ω and a few kΩ, thus most of the microwave (MW) power is reflected due to the impedance mismatch between the bar and the MW source ($Z_{\mathrm{out}} = 50$ Ω). To calibrate MW current, we make use of the Joule heating. The amount of heating is measured using the change of resistance. First, a dc current is swept from large negative to large positive values and the differential resistance is measured, giving the resistance change due to dc heating. Then we measure the resistance change with increasing microwave power. The example measurements for a 500-nm wide and 5-μm long bar of Ru(3)/IrMn(2)/Py(4)/Al(2) are plotted in Fig. 8(a). For dc, the value of current is known because it is all dissipated in the bar, there are no reflections. We are able to find the current for each applied MW power by comparing the MW and dc heatings. In Fig. 8(b), we plot the values of dc current causing the same amount of heating as MW powers on the x axis. The corresponding MW current is $\sqrt{2}$ times the dc current, because the heating for the ac current is given by $I^2R/2$ compared to

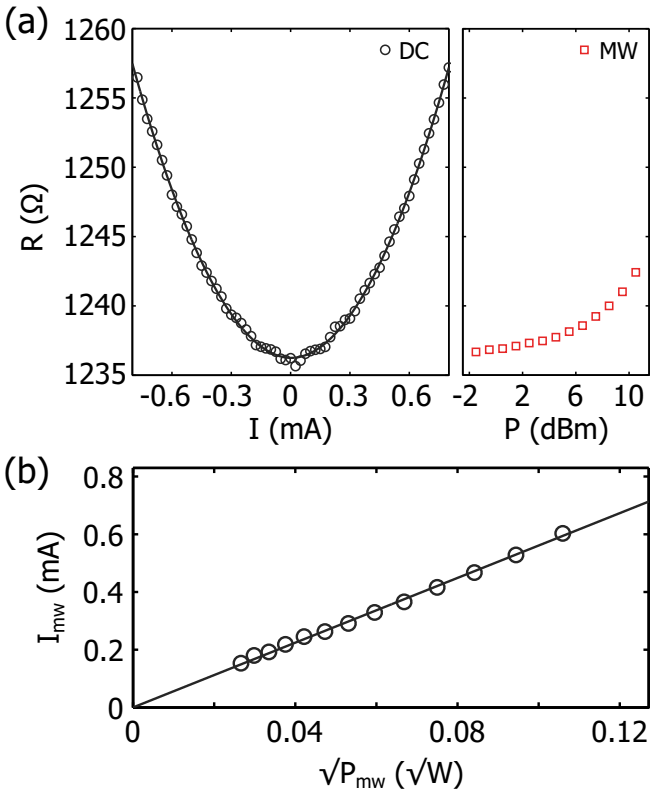

FIG. 8. (Color online) (a) Comparison of resistance change due to heating caused by dc (left) and MW (right) currents. The dc measurement is symmetric with respect to 0 current. (b) MW current vs square root of applied MW power obtained from the heating calibration. The solid line is a linear fit to the data (circles).

I^2R for dc (this is already taken into account in the plot). As expected, MW current is linear with the square root of power (in W). From the linear fit, we can extract the value of MW current per square root of power.

APPENDIX B: LAYER RESISTIVITIES AND OERSTED FIELD

One can not use the bulk resistivities of individual metals for the estimation of the current distribution. The values change dramatically for thin layers. Additionally, there is a contact resistance which has to be taken into account. These values can be determined by a careful analysis of bars with different dimensions and layer thicknesses. In Fig. 9(a), we plot resistances of 4-μm -wide bars of 40-, 80-, and 120-μm lengths. The intersection of the linear fit with y axis is the average contact resistance, $R_{\rm cont} = 235 \pm 75\ \Omega$. In Fig. 9(b), we plot resistances of bars with the same dimensional ratio but different IrMn thicknesses d_A in Ru(3)/IrMn(d_A)/NiFe(4) structures. The average contact resistance has been subtracted. We neglect the 2-nm Al capping layer as it is the same for all the samples and is believed to be mainly oxidized. The samples with 3–8-nm IrMn fit well to a simple model of parallel resistors, given by

$$R = R_{\rm cont} + \frac{b\,\rho_{\rm IrMn}}{d_A + b\,\rho_{\rm IrMn}/r}, \qquad \text{(B1)}$$

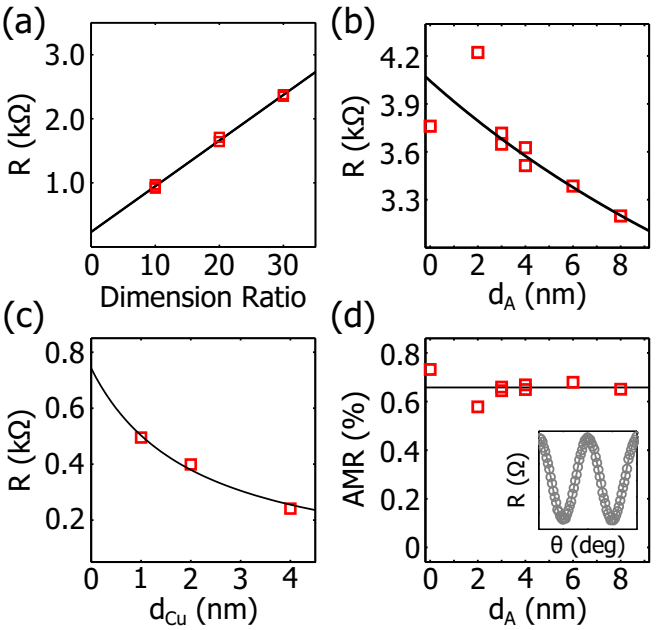

FIG. 9. (Color online) (a) Resistances of bars with different length/width ratios. The fit to a line gives the average contact resistance. (b) Resistances of bars with the same dimension ratio 60 but different IrMn thicknesses. Resistances of 3–8-nm samples are fitted to Eq. (B1) (solid like). (c) Resistances of bars with different Cu spacer thicknesses fitted to Eq. (B1). (d) The magnitude of intrinsic AMR of NiFe in samples with different IrMn thicknesses, extracted using Eq. (B5). In the inset, we show a typical measurement for extracting the total AMR $\Delta R_{\rm tot}$.

where b is the length/width ratio of the bars (60 for this set of samples) and r is the resistance of the multilayer without IrMn. The fit gives $\rho_{\rm IrMn} = 20.5 \pm 3.5 \times 10^{-7}\ \Omega\,{\rm m}$. One can also see that the resistance of the sample with 0-nm IrMn is smaller than that of the sample with 2-nm IrMn. We believe this is due to the higher resistivity of NiFe grown on IrMn compared to that of NiFe grown on Ru. It is known that NiFe can have different resistivities depending on the seed layer [46–48]. This fact is more pronounced for the 2-nm IrMn thickness, where the resistivity of NiFe is the highest. Using samples with different Ru thicknesses we find $\rho_{\rm Ru} = 4.0 \pm 0.3 \times 10^{-7}\ \Omega\,{\rm m}$ and $\rho_{\rm NiFe}^{\rm Ru} = 4.7 \pm 0.3 \times 10^{-7}\ \Omega\,{\rm m}$ for NiFe grown on Ru. Using the resistivity of IrMn obtained earlier and the value of $\rho_{\rm Ru}$ we find $\rho_{\rm NiFe}^{\text{2-nm IrMn}} = 6.9 \pm 0.6 \times 10^{-7}\ \Omega\,{\rm m}$ and $\rho_{\rm NiFe}^{\rm IrMn} = 5.4 \pm 0.4 \times 10^{-7}\ \Omega\,{\rm m}$. The resistivity of Cu is deduced from the Ru(3)/IrMn(4)/Cu($d_{\rm Cu}$)/Py(4) structures, where $d_{\rm Cu}$ is 1, 2, or 4 nm [Fig. 9(c)]. We find $\rho_{\rm Cu} = 1.55 \times 10^{-7}\ \Omega\,{\rm m}$.

To verify the parallel resistors approach, we compare values of AMR for layers with different IrMn thicknesses. Change of the resistance due to AMR is extracted by rotating the direction of the magnetic field with respect to the sample [see the inset of Fig. 9(d)]. The value of measured net AMR depends on the proportion of the current in the NiFe layer and the size of its AMR. Below, we deduce the exact relationship for the parallel resistors model:

$$R_{\rm tot} = (1/R_{\rm NiFe} + 1/R_{\rm rest})^{-1} = \frac{R_{\rm NiFe}\,R_{\rm rest}}{R_{\rm NiFe} + R_{\rm rest}}, \qquad \text{(B2)}$$

$$\Delta R_{\rm tot} = \frac{(R_{\rm NiFe}+\Delta R_{\rm NiFe})R_{\rm rest}}{R_{\rm NiFe}+\Delta R_{\rm NiFe}+R_{\rm rest}} - \frac{R_{\rm NiFe}R_{\rm rest}}{R_{\rm NiFe}+R_{\rm rest}} \approx \frac{\Delta R_{\rm NiFe}R_{\rm rest}^2}{(R_{\rm NiFe}+R_{\rm rest})^2}, \quad \text{(B3)}$$

$$\frac{\Delta R_{\rm tot}}{R_{\rm tot}} \approx \Delta R_{\rm NiFe}\frac{R_{\rm tot}}{R_{\rm NiFe}^2}, \quad \text{(B4)}$$

$$\frac{\Delta R_{\rm NiFe}}{R_{\rm NiFe}} = R_{\rm NiFe}\frac{\Delta R_{\rm tot}}{R_{\rm tot}^2}. \quad \text{(B5)}$$

Therefore $R_{\rm NiFe}\frac{\Delta R_{\rm tot}}{R_{\rm tot}^2}$ can be used to determine the value of AMR in NiFe. In Fig. 9(d), we plot this quantity for the measured IrMn thicknesses. As one can see it is almost the same (0.7%) for the 3–8-nm thickness range of IrMn. For the sample with 2-nm IrMn the AMR of NiFe is slightly smaller, whereas it is slightly larger for NiFe grown on Ru. Decrease of intrinsic AMR of NiFe for thin layers, as well as its dependence on the seed layer has been reported previously [47,49–51]. The agreement of AMR magnitudes supports the parallel resistors approach and suggests that the estimates of layer resistivities are correct.

As yet another additional supporting argument for our estimates, the bulk resistivity ratio is approximately 18(IrMn) : 1(Ru) : 2(NiFe), using values 1260×10^{-7}, 71×10^{-7}, and 140×10^{-7} Ω m [52–54]. The ratios of resistivities deduced here are 5.1 : 1 : 1.2–1.8. The relative order is the same, but differences in resistivities are more moderate because of the substantial interfacial scattering for thin films, making the resistivity less material-dependent.

Current in the IrMn, Ru and Cu layers creates an effective Oersted field in the y direction at the center of the NiFe layer. The current in the NiFe itself generates only a symmetric Oersted field with respect to the center of the layer which does not contribute to the effective h_y or h_z (Fig. 10). From Ampere's law, we have

$$\oint h_{\rm Oe}{\rm d}l = I. \quad \text{(B6)}$$

Where I is the current encircled by the integration loop. For our geometry, we can write

$$\mu_0 h_{\rm Oe} = \frac{\mu_0 I_{\rm Oe}}{2(w+d)} \approx \frac{\mu_0 I_{\rm Oe}}{2w}. \quad \text{(B7)}$$

Here, $I_{\rm Oe}$ is the current in the Ru, IrMn, and Cu layers. We used the fact that the thickness d of the bar (~10 nm) is very small compared to its width w (500 nm–4 μm) for all measured devices. This means that the Oersted field depends only on the size of the current in Ru, IrMn, and Cu layers, and not on layer thicknesses, similar to the case of an infinite plane.

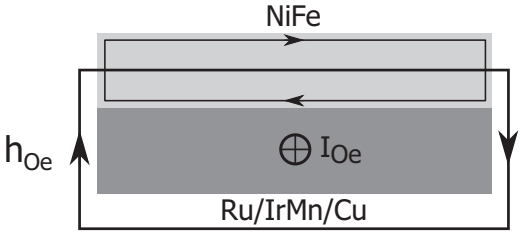

FIG. 10. Schematic representation of the Oersted fields induced by the current in the multilayer.

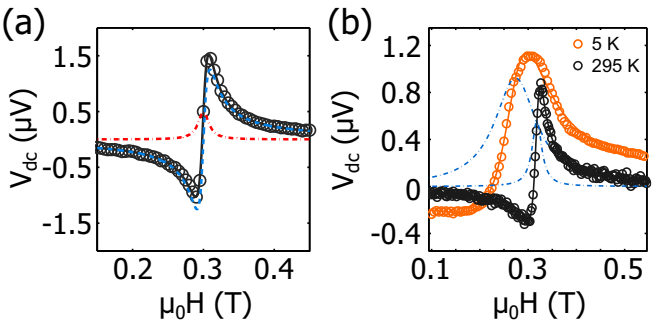

FIG. 11. (Color online) (a) A resonance curve measured in a Ru(3)Py(4) bar at 17.9 GHz, decomposed into symmetric and antisymmetric Lorentzians. (b) Resonances measured in the 3-nm IrMn sample at 5 K and in the 2-nm IrMn sample at room temperature (295 K), at 16.5 and 18.6 GHz microwave frequencies, respectively. The antisymmetric components are normalized to 1 μV (not shown), and the symmetric components are shown with dotted lines.

APPENDIX C: THE ROLE OF THE SEED LAYER

In Fig. 11(a), we plot a typical FMR measurement in a SiO_x/Ru(3)/Py(4)/Al(2) structure. As one can see the symmetric component is small and the spin-Hall angle of 0.009 is extracted from the h_z/h_y ratio using

$$\theta_{\rm SH} = \frac{h_z}{h_y}\frac{e\mu_0 M_s d_{\rm Ru} d_{\rm NiFe}}{\hbar}. \quad \text{(C1)}$$

To additionally confirm the fact that the seed layer does not have a major contribution, we measure structures with 4.5-nm Ta seed layer instead of Ru, with 2- and 3-nm IrMn, both at room temperature and at 5 K. Neither 2- nor 3-nm IrMn samples exhibit exchange bias at room temperature. The 2-nm IrMn sample does not develop any substantial exchange bias even at low temperatures, whereas the 3-nm IrMn sample develops an exchange bias of 8 ± 1 mT at 5 K. In Fig. 11(b), we plot typical resonances measured at these samples. Firstly, in both cases the symmetric component is positive. Ta has a large negative spin-Hall angle and if the effect was due to the spin-current from Ta, one would expect h_z and thus the symmetric component to be negative for a positive antisymmetric component. Additionally, one can see that at low temperature the symmetric component becomes even larger, further supporting the argument that the increase of the antidamping torque is not related to the efficiency of the transfer of the spin-current induced in the seed layer, as this would lead to a decrease of h_z for Ta.

APPENDIX D: POWER, FREQUENCY, AND DIMENSION DEPENDENCE OF CURRENT-INDUCED TORQUES.

In Fig. 12(a), we show the power dependence of the magnitudes of symmetric and antisymmetric Lorentzians as well as their ratio for the 2-nm IrMn sample measured at 17.9 GHz. As one can see, both symmetric and antisymmetric components scale linearly with power, as expected for the rectification signal (h, I $\propto \sqrt{P}$, see equations (1) and (2) in the main

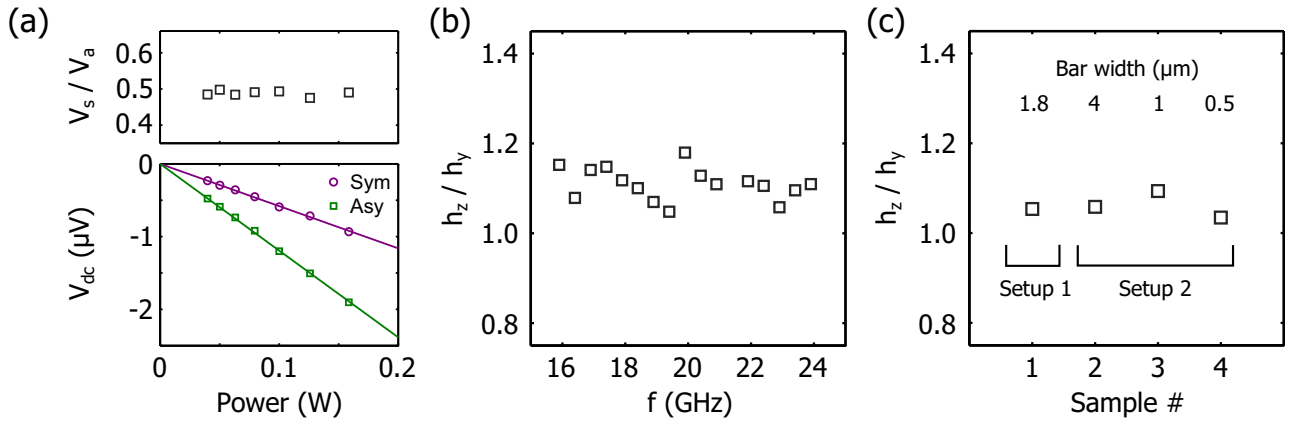

FIG. 12. (Color online) (a) Dependence of $V_{\rm sym}$ and $V_{\rm asy}$ and their ratio on applied microwave power for the 2-nm IrMn sample. Solid lines are linear fits. (b) Frequency dependence of the h_z/h_y ratio for the 3-nm IrMn sample. (c) h_z/h_y ratio for 2-nm IrMn samples with different dimensions and measured in two different setups. The bar dimensions are 1.8 μm × 38 μm, 4 μm × 240 μm, 1 μm × 10 μm, and 500 nm × 5 μm.

text). Their ratio is power independent. In Fig. 12(c), we show that the h_z / h_y ratio is frequency independent in our devices. The data shown are for the 3-nm IrMn sample. Note that here the ratio is extracted from single resonances rather than a full angle-dependent measurement, thus the relatively large fluctuations, although still within about 10% of each other.

Some of the measurements were performed in bars with different dimensions to exclude any geometry related effects. Parts of measurements were also performed in two different measurement systems, with the same results. Figure 12(d) summarizes the above stated for the 2-nm IrMn sample.

APPENDIX E: MAGNETIC ANISOTROPIES: $A_{\rm sym}$ AND $A_{\rm asy}$

The total magnetic anisotropy is modeled as a combination of unidirectional, uniaxial and rotational anisotropies. Unidirectional anisotropy models the exchange bias. Uniaxial anisotropy is a combination of shape anisotropy, crystalline anisotropy of NiFe and some uniaxial anisotropy due to the exchange bias [35]. The contribution of each of these towards the cumulative uniaxial anisotropy can vary depending on the dimensions of the bar and the thickness of the IrMn layer, however, we find that for our samples the uniaxial anisotropy is dominated by the shape anisotropy. Rotational anisotropy is due to the partially stable grains of the polycrystalline IrMn coupling to the NiFe at the interface. These are the same AFM grains responsible for the increased coercivity of magnetic hysteresis measurements [35]. This anisotropy is modeled as an additional isotropic in-plane effective field $H_{\rm rot}$ along the NiFe magnetizatoin direction. Magnetic free energy per unit area becomes

$$\begin{aligned} F[\theta,\phi] &= F_{\rm Zeeman}[\theta,\phi] + F_{\rm surf}[\theta,\phi] + F_{\rm shape}[\theta,\phi] \\ &\quad + F_U[\theta,\phi] + F_{\rm exch}[\theta,\phi] \\ &= \mu_0(H + H_{\rm rot})Md_F(\sin\phi\sin\phi_H\cos(\theta-\theta_H) \\ &\quad + \cos\phi\cos\phi_H) + (\mu_0 M^2 d_F/2 - K_S)\cos^2\phi \\ &\quad - K_U d_F \sin^2\phi\cos^2(\theta-\theta_{\rm uni}) \\ &\quad - \mu_0 M d_F H_{\rm ex}\cos(\theta-\theta_{\rm exch})\sin\phi, \end{aligned} \tag{E1}$$

where (θ_H, ϕ_H) and (θ, ϕ) are in- and out-of-plane angles of applied field H and magnetization M in spherical coordinates, with $\phi = 90^\circ$ being in the plane of the sample. K_S and K_U are surface and in-plane uniaxial anisotropy constants, d_F is the thickness of the ferromagnetic layer, $H_{\rm ex}$ is the exchange bias field, $\theta_{\rm uni}$ and $\theta_{\rm exch}$ are directions of the uniaxial anisotropy and the exchange bias, respectively. The resonance condition reads

$$\left(\frac{\omega}{\gamma}\right)^2 = \frac{1}{M^2 d_F^2 \sin^2\theta}\left[\left(\frac{\partial^2 F}{\partial\theta^2}\right)\left(\frac{\partial^2 F}{\partial\phi^2}\right) - \left(\frac{\partial^2 F}{\partial\phi\partial\theta}\right)^2\right], \tag{E2}$$

where ω is the resonance frequency and γ is the gyromagnetic ratio. Plugging in the expression for $F[\theta,\phi]$ into the equation above and differentiating it with respect to θ and ϕ one obtains

$$\left(\frac{\omega}{\gamma}\right)^2 = \mu_0^2(H + H_1)(H + H_2) \tag{E3}$$

with

$$\begin{aligned} H_1 &= H_{\rm rot} + M_{\rm eff} + H_{\rm exch}\cos(\theta-\theta_{\rm exch}) + H_U\cos^2(\theta-\theta_U), \\ H_2 &= H_{\rm rot} + H_{\rm exch}\cos(\theta-\theta_{\rm exch}) + H_U\cos[2(\theta-\theta_U)]. \end{aligned} \tag{E4}$$

Here we have relabeled the variables in the following way:

$$\begin{aligned} M_{\rm eff} &= M - 2K_S/\mu_0 M d_F, \\ H_U &= 2K_U/\mu_0 M. \end{aligned} \tag{E5}$$

We use Eq. (E3) to fit the in-plane angle dependence of the resonance field and extract anisotropies of each sample. In this model $M_{\rm eff}$ and $H_{\rm rot}$ are correlated, so we need to know one of these using a different method. This correlation is easier to see if we rewrite Eq. (E3) making an approximation $H_{\rm res} + H_1 \approx M_{\rm eff}$. This is valid because the rest of the terms in H_1 are much

smaller than $M_{\rm eff}$. We write (E3) as

$$\mu_0 H_{\rm res} = \left(\frac{\omega}{\gamma}\right)^2 \frac{1}{\mu_0 M_{\rm eff}} - \mu_0 H_{\rm rot} - \mu_0 H_{\rm exch}\cos(\theta - \theta_{\rm exch}) - \mu_0 H_U \cos[2(\theta - \theta_U)]. \quad \text{(E6)}$$

For the given frequency, larger $M_{\rm eff}$ leads to a smaller $H_{\rm rot}$ and vice versa. We extract $M_{\rm eff}$ from the frequency dependence of the resonance field and use it to fit out $H_{\rm rot}$ (the fitting is done using the full model and not the approximation).

$A_{\rm sym}$ and $A_{\rm asy}$ entering the expressions for the rectified dc voltage are given by

$$A_{\rm sym} = \frac{\gamma(H_{\rm res}+H_1)(H_{\rm res}+H_2)}{\omega\Delta H(2H_{\rm res}+H_1+H_2)}, \qquad A_{\rm asy} = \frac{(H_{\rm res}+H_1)}{\mu_0\Delta H(2H_{\rm res}+H_1+H_2)}, \quad \text{(E7)}$$

as deduced in Ref. [23], with H_1 and H_2 given by Eq. (E4), and ΔH being the resonance linewidth.

[1] A. Núñez, R. Duine, P. Haney, and A. MacDonald, Phys. Rev. B **73**, 214426 (2006).
[2] P. Haney and A. MacDonald, Phys. Rev. Lett. **100**, 196801 (2008).
[3] Y. Xu, S. Wang, and K. Xia, Phys. Rev. Lett. **100**, 226602 (2008).
[4] H. V. Gomonay, Phys. Rev. B **81**, 144427 (2010).
[5] K. Hals, Y. Tserkovnyak, and A. Brataas, Phys. Rev. Lett. **106**, 107206 (2011).
[6] A. B. Shick, S. Khmelevskyi, O. N. Mryasov, J. Wunderlich, and T. Jungwirth, Phys. Rev. B **81**, 212409 (2010).
[7] J. Železný, H. Gao, K. Výborný, J. Zemen, J. Mašek, A. Manchon, J. Wunderlich, J. Sinova, and T. Jungwirth, Phys. Rev. Lett. **113**, 157201 (2014).
[8] J. Nogués and I. K. Schuller, J. Magn. Magn. Mater. **192**, 203 (1999).
[9] B. G. Park, J. Wunderlich, X. Martí, V. Holý, Y. Kurosaki, M. Yamada, H. Yamamoto, A. Nishide, J. Hayakawa, H. Takahashi, A. B. Shick, and T. Jungwirth, Nat. Mater. **10**, 347 (2011).
[10] Y. Y. Wang, C. Song, B. Cui, G. Y. Wang, F. Zeng, and F. Pan, Phys. Rev. Lett. **109**, 137201 (2012).
[11] X. Marti, I. Fina, C. Frontera, J. Liu, P. Wadley, Q. He, R. J. Paull, J. D. Clarkson, J. Kudrnovský, I. Turek, J. Kuneš, D. Yi, J.-H. Chu, C. T. Nelson, L. You, E. Arenholz, S. Salahuddin, J. Fontcuberta, T. Jungwirth, and R. Ramesh, Nat. Mater. **13**, 367 (2014).
[12] I. Fina, X. Marti, D. Yi, J. Liu, J. H. Chu, C. Rayan-Serrao, S. Suresha, a. B. Shick, J. Zelezný, T. Jungwirth, J. Fontcuberta, and R. Ramesh, Nat. Commun. **5**, 4671 (2014).
[13] P. Wadley, B. Howells, J. Zelezny, C. Andrews, V. Hills, R. P. Campion, V. Novak, F. Freimuth, Y. Mokrousov, A. W. Rushforth, K. W. Edmonds, B. L. Gallagher, and T. Jungwirth, arXiv:1503.03765.
[14] H. Wang, C. Du, P. C. Hammel, and F. Yang, Phys. Rev. Lett. **113**, 097202 (2014).
[15] C. Hahn, G. de Loubens, V. V. Naletov, J. Ben Youssef, O. Klein, and M. Viret, Europhys. Lett. **108**, 57005 (2014).
[16] T. Moriyama, M. Nagata, K. Tanaka, K.-j. Kim, H. Almasi, and W. G. Wang, arXiv:1411.4100.
[17] D. Ralph and M. Stiles, J. Magn. Magn. Mater. **320**, 1190 (2008).
[18] J. B. S. Mendes, R. O. Cunha, O. Alves Santos, P. R. T. Ribeiro, F. L. A. Machado, R. L. Rodríguez-Suárez, A. Azevedo, and S. M. Rezende, Phys. Rev. B **89**, 140406 (2014).
[19] W. Zhang, M. B. Jungfleisch, W. Jiang, J. E. Pearson, A. Hoffmann, F. Freimuth, and Y. Mokrousov, Phys. Rev. Lett. **113**, 196602 (2014).
[20] B. A. Bernevig and O. Vafek, Phys. Rev. B **72**, 033203 (2005).
[21] A. Manchon and S. Zhang, Phys. Rev. B **78**, 212405 (2008).
[22] A. Chernyshov, M. Overby, X. Liu, J. K. Furdyna, Y. Lyanda-Geller, and L. P. Rokhinson, Nat. Phys. **5**, 656 (2009).
[23] D. Fang, H. Kurebayashi, J. Wunderlich, K. Výborný, L. P. Zârbo, R. P. Campion, A. Casiraghi, B. L. Gallagher, T. Jungwirth, and A. J. Ferguson, Nat. Nanotechnol. **6**, 413 (2011).
[24] I. M. Miron, G. Gaudin, S. Auffret, B. Rodmacq, A. Schuhl, S. Pizzini, J. Vogel, and P. Gambardella, Nat. Mater. **9**, 230 (2010).
[25] I. M. Miron, K. Garello, G. Gaudin, P.-J. Zermatten, M. V. Costache, S. Auffret, S. Bandiera, B. Rodmacq, A. Schuhl, and P. Gambardella, Nature (London) **476**, 189 (2011).
[26] L. Liu, C.-F. Pai, Y. Li, H. W. Tseng, D. C. Ralph, and R. A. Buhrman, Science **336**, 555 (2012).
[27] K. Garello, I. M. Miron, C. O. Avci, F. Freimuth, Y. Mokrousov, S. Blügel, S. Auffret, O. Boulle, G. Gaudin, and P. Gambardella, Nat. Nanotechnol. **8**, 587 (2013).
[28] H. Kurebayashi, J. Sinova, D. Fang, A. C. Irvine, T. D. Skinner, J. Wunderlich, V. Novák, R. P. Campion, B. L. Gallagher, E. K. Vehstedt, L. P. Zârbo, K. Výborný, A. J. Ferguson, and T. Jungwirth, Nat. Nanotechnol. **9**, 211 (2014).
[29] M. V. Costache, S. M. Watts, M. Sladkov, C. H. van der Wal, and B. J. van Wees, Appl. Phys. Lett. **89**, 232115 (2006).
[30] S. Yakata, Y. Ando, T. Miyazaki, and S. Mizukami, Jpn. J. Appl. Phys. **45**, 3892 (2006).
[31] S. Nicolodi, L. C. C. M. Nagamine, a. D. C. Viegas, J. E. Schmidt, L. G. Pereira, C. Deranlot, F. Petroff, and J. Geshev, J. Magn. Magn. Mater. **316**, 97 (2007).
[32] L. Liu, T. Moriyama, D. Ralph, and R. Buhrman, Phys. Rev. Lett. **106**, 036601 (2011).
[33] T. Tanaka, H. Kontani, M. Naito, T. Naito, D. S. Hirashima, K. Yamada, and J. Inoue, Phys. Rev. B **77**, 165117 (2008).
[34] R. Acharyya, H. Y. T. Nguyen, W. P. Pratt, and J. Bass, J. Appl. Phys. **109**, 07C503 (2011).
[35] M. D. Stiles and R. D. McMichael, Phys. Rev. B **59**, 3722 (1999).
[36] M. D. Stiles and R. D. McMichael, Phys. Rev. B **63**, 064405 (2001).
[37] M. Ali, C. H. Marrows, M. Al-Jawad, B. J. Hickey, A. Misra, U. Nowak, and K. D. Usadel, Phys. Rev. B **68**, 214420 (2003).
[38] J. McCord, R. Mattheis, and D. Elefant, Phys. Rev. B **70**, 094420 (2004).
[39] J. Kim, J. Sinha, S. Mitani, M. Hayashi, S. Takahashi, S. Maekawa, M. Yamanouchi, and H. Ohno, Phys. Rev. B **89**, 174424 (2014).
[40] Y. Tserkovnyak, A. Brataas, and G. E. W. Bauer, Phys. Rev. B **66**, 224403 (2002).

[41] S. M. Rezende, A. Azevedo, M. A. Lucena, and F. M. de Aguiar, Phys. Rev. B **63**, 214418 (2001).
[42] S. Yuan, B. Kang, L. Yu, S. Cao, and X. Zhao, J. Appl. Phys. **105**, 063902 (2009).
[43] Z. Wei, A. Sharma, A. Nunez, P. Haney, R. Duine, J. Bass, A. MacDonald, and M. Tsoi, Phys. Rev. Lett. **98**, 116603 (2007).
[44] S. Urazhdin and N. Anthony, Phys. Rev. Lett. **99**, 046602 (2007).
[45] W. Zhang, M. B. Jungfleisch, F. Freimuth, W. Jiang, J. Sklenar, J. E. Pearson, J. B. Ketterson, Y. Mokrousov, and A. Hoffmann, Phys. Rev. B **92**, 144405 (2015).
[46] B. Warot, J. Imrie, a.K Petford-Long, J. Nickel, and T. Anthony, J. Magn. Magn. Mater. **272-276**, E1495 (2004).
[47] H. Gong, D. Litvinov, T. Klemmer, D. Lambeth, and J. Howard, IEEE Trans. Magn. **36**, 2963 (2000).
[48] L. Jin, H. Zhang, X. Tang, F. Bai, and Z. Zhong, J. Appl. Phys. **113**, 053902 (2013).
[49] T. Yeh, J. Sivertsen, and J. Judy, IEEE Trans. Magn. **23**, 2215 (1987).
[50] T. Rijks and R. Coehoorn, Phys. Rev. B **51**, 283 (1995).
[51] G. Choe and M. Steinback, J. Appl. Phys. **85**, 5777 (1999).
[52] R. Acharyya, Ph.D. thesis, Michigan State University, 2012.
[53] J. Choi, Y. Choi, J. Hong, H. Tian, J.-S. Roh, Y. Kim, T.-M. Chung, Y. W. Oh, Y. Kim, C. G. Kim, and K. No, Jpn. J. Appl. Phys. **41**, 6852 (2002).
[54] A. F. Mayadas, J. Appl. Phys. **45**, 2780 (1974).